Sea ice leads in the Arctic Ocean: Model assessment, interannual variability and trends

Q. Wang,[1] S. Danilov,[1] T. Jung,[1,2] L. Kaleschke[3], and A. Wernecke[3]

Key points.

- Arctic leads can be simulated by increasing resolution (4.5 km) and ensuring numerical convergence
- The model represents the observed spatial and temporal variability of ice leads well
- There is no significant recent trend in lead area fraction during wintertime

---

Corresponding author: Q. Wang, Alfred Wegener Institute Helmholtz Centre for Polar and Marine Research, Bremerhaven, Germany (Qiang.Wang@awi.de)

[1]Alfred Wegener Institute Helmholtz Centre for Polar and Marine Research, Bremerhaven, Germany

[2]Institute of Environmental Physics, University of Bremen, Bremen, Germany

[3]Institute of Oceanography, University of Hamburg, Hamburg, Germany

Sea ice leads in the Arctic are important features that give rise to strong localized atmospheric heating; they provide the opportunity for vigorous biological primary production; and predicting leads may be of relevance for Arctic shipping. It is commonly believed that traditional sea ice models that employ elastic-viscous-plastic (EVP) rheologies are not capable of properly simulating sea ice deformation, including lead formation, and thus new formulations for sea ice rheologies have been suggested. Here we show that classical sea ice models have skill in simulating the spatial and temporal variation of lead area fraction in the Arctic when horizontal resolution is increased (here 4.5 km in the Arctic) and when numerical convergence in sea ice solvers is considered, which is frequently neglected. The model results are consistent with satellite remote sensing data and discussed in terms of variability and trends of Arctic sea ice leads. It is found, for example, that wintertime lead area fraction during the last three decades has not undergone significant trends.

1. Introduction

Sea ice is an important component of the Earth System, which is often being discussed in terms of integrated quantities such as Arctic sea ice extent and volume. Sea ice deformation characteristics such as leads, on the other hand, have attracted relatively little attention thus far. Leads may play an important role, despite of the fact that they cover only a relatively small fraction of the total Arctic sea ice area. Air-sea interaction is significantly reduced by sea ice, leaving the fluxes mainly in the area of leads, where there is open water or thin ice [*Maykut*, 1978]. In fact, turbulent heat transfer between the ocean and atmosphere is known to depend on the details of leads [*Marcq and Weiss*, 2012], with small changes in the lead fraction having the potential to induce sizable temperature changes in the atmospheric boundary layer [*Lüpkes et al.*, 2008]. Furthermore, increasing sea ice deformation and lead opening can accelerate sea ice thinning through the sea ice-albedo feedback [*Rampal et al.*, 2009]. Leads have also been associated with enhanced methane emission in the Arctic Ocean [*Kort et al.*, 2012] and changed mercury as well as ozone concentrations in the atmospheric boundary layer [*Moore et al.*, 2014]. Finally, information on sea ice deformation, including leads, is important for Arctic shipping [*Jung et al.*, 2016].

Despite of the importance of sea ice leads, relatively little is known on how well they can be represented by commonly used sea ice models. A number of studies concluded that leads and sea ice linear kinematic features cannot be well simulated by traditional sea ice models [*Lindsay et al.*, 2003; *Kwok et al.*, 2008; *Girard et al.*, 2009]. This may partly explain why there has been a quest for new sea ice model rheologies in recent years [see, e.g., *Girard et al.*, 2011; *Tsamados et al.*, 2013; *Bouillon and Rampal*, 2015]. The lack of existing modelling capacity has meant that our understanding of linear kinematics of sea ice is mainly based on buoys and satellite observations of ice drift [e.g., *Kwok et al.*, 1998; *Lindsay*, 2002; *Weiss and Marsan*, 2004; *Marsan et al.*, 2004; *Rampal et al.*, 2009; *Stern and Lindsay*, 2009; *Hutchings et al.*, 2011; *Herman and Glowacki*, 2012] and satellite as well as airborne measurements for sea ice leads [*Fily and Rothrock*, 1990; *Stone and Key*, 1993; *Lindsay and Rothrock*, 1995; *Miles and Roger*, 1998; *Tschudi et al.*, 2002; *Onana et al.*, 2013; *Broehan and Kaleschke*, 2014; *Willmes and Heinemann*, 2015, 2016]. Here, we exploit the fact that lead area fraction datasets for the last decade have become available [*Roehrs and Kaleschke*, 2012; *Wernecke and Kaleschke*, 2015; *Willmes and Heinemann*, 2015, 2016; *Ivanov et at.*, 2016], which can be used to evaluate sea ice models.

The goal of this work is to show that sea ice linear kinematic features can be simulated by the traditional sea ice models with a certain skill. The prerequisite is a sufficiently high horizontal resolution along with numerical convergence of sea ice solvers which is frequently neglected. We simulate Arctic sea ice using the elastic-visco-plastic (EVP) approach [*Hunke and Dukowicz*, 1997] in a global sea ice ocean model at a local resolution of 4.5 km and show that many characteristics of the simulated leads agree with the available observations already at this resolution. This allows us to discuss the variability and trend of the lead features from long model-generated time series.

2. Method

All simulations described in this study were performed with the Finite Element Sea-ice Ocean Model [FESOM, see *Wang et al.*, 2014], which is the first mature global sea ice-ocean model that is formulated on unstructured meshes, including its sea ice component [Finite Element Sea Ice Model, FESIM, see *Danilov et al.*, 2015]. The model is discretized on triangles and characterized by the collocated placement of ocean and sea ice variables. It is used in the coupled Alfred Wegener Institute (AWI) climate model [*Sidorenko et al.*, 2015].

We used a global configuration with nominal horizontal resolution of about 1 degree for most of the global ocean; north of 45°N the horizontal resolution was increased to 24 km; and starting from the Arctic gateways (Fram Strait, Barents Sea Opening, Bering Strait, and the Canadian Arctic Archipelago) the resolution was further refined to 4.5 km. An updated version of the *Hunke and Dukowicz* [1997] EVP method was used in this study in which all the components of the stress tensor are relaxed to their viscous-plastic state at the same rate [see *Danilov et al.*, 2015]. This approach dramatically improves stability and leads to results that are very similar to those obtained with the modified EVP method proposed by *Bouillon et al.* [2013]. Importantly, we used 800 subcycling time steps in the EVP solver to warrant noise-free ice velocity divergence and shear.

The model was forced using atmospheric state variables from the NCEP/NCAR Reanalysis [*Kalnay et al.*, 1996]. The spinup was done for the period 1948 to 1977 on another, coarser mesh without refinement to 4.5 km in the Arctic Ocean. At the end of the spin-up the data were interpolated to the fine mesh and the model was further run until 2014. The results of this study are based on the last 30 years (1985–2014) of the high-resolution simulation with Arctic refinement.

In this work satellite data are used to assess the realism of the model in simulating leads in the Arctic. The winter sea ice deformation fields based on the well established RADARSAT Geophysical Processor System (RGPS) [*Kwok et al.*, 1998] are employed. RGPS resolves sea ice fractures at about 10 km resolution and provides deformation data for the period of 1997–2008. Furthermore, the following three datasets of lead area fraction are used in our work. Passive microwave images from the Advanced Microwave Scanning Radiometer-Earth Observation System (AMSR-E) allow daily observations of sea ice leads at about 6 km resolution. A dataset of daily Arctic lead area fraction for wintertime based on AMSR-E is available for the period 2002 to 2011 [*Roehrs and Kaleschke*, 2012]. Lead detection based on CryoSat-2 measurements (with resolutions of a few hundred meters to about one kilometer) shows in some regions more reasonable results than AMSR-E [*Wernecke and Kaleschke*, 2015] and extends the lead fraction dataset (winter monthly means) to recent years. *Willmes and Heinemann* [2015, 2016] provide a nearly 1 km resolution lead detection product from the Moderate Resolution Imaging Spectroradiometer (MODIS) measurements. The MODIS daily data of lead area fraction (defined here as the fraction of ensured lead detections from all data points not identified as cloud) are available for wintertime starting from 2003.

3. Results

A snapshot of the simulated sea ice concentration and thickness on 1 January 2004 is shown in Fig. 1a. Evidently, the model captures many long and narrow cracks, which are typical features observed in sea ice [e.g., *Wernecke and Kaleschke*, 2015; *Willmes and Heinemann*, 2016]. For this particular case, cracks are mainly located in Beaufort Sea and near Fram Strait. Very long cracks are also visible in the region of thick sea ice north of the Canadian Arctic Archipelago (CAA). The high resolution (4.5 km) used in the simulation is crucial for the model's capability to generate these small scale features. To substantiate this point, the sea ice thickness on the same day, simulated on a coarser (24 km) grid, is shown in Fig. 1b. The coarse model simulates a much smoother ice thickness field without the narrow crack structures obtained on the high resolution mesh. There is some indication of ice breakup on the coarse grid; for example, there is evidence for cracks north of the CAA, which are approximately at the same location as those obtained on the high resolution mesh. However, these features are much wider and less pronounced than those obtained at high resolution. Our results are in general agreement with previous modelling studies, which have also indicated that narrow cracks start to emerge when model resolution is increased [e.g., *Maslowski and Lipscomb*, 2003].

Importantly, to exploit the full potential of classical sea ice models in representing leads, only increasing resolution is not sufficient. It is necessary to ensure EVP solver convergence, which can be achieved through modifications to the EVP solver along with an increased number of subcycling steps (Fig. 1c and Fig. S1 in the supplementary material).

We identify leads from the simulated ice thickness field to quantify lead area fraction. The model resolution of 4.5 km is not fine enough to resolve narrow leads well, so many of the leads in the model appear as linear features of reduced thickness rather than fully open water. We define leads as locations where sea ice is at least 20% thinner than at its surroundings (within a radius of 25 km, so very wide leads are excluded). The threshold value of 20% allows to capture most of the visually apparent linear features in sea ice thickness (see Fig. S2 in the supplement), and it also makes the magnitude of the simulated lead area fraction close to the observations. Although the good match of the magnitude of lead area fraction between the model and observations shown below partly comes from tuning the threshold, the derived variability and trend of lead area fraction is not sensitive to reasonable changes in the threshold used (see Fig. S3). In this study the focus is on the spatial and temporal variation of lead area fraction.

The observed mean wintertime lead area fraction, obtained from CryoSat-2 and MODIS for the period 2011–14 [*Wernecke and Kaleschke*, 2015; *Willmes and Heinemann*, 2015], is shown in Fig. 2a. The largest lead area fraction is observed in the coastal regions, including Fram Strait, Barents Sea, Kara Sea, Laptev Sea, and Beaufort Sea; smaller values are found in the interior of the Arctic. Overall, the model reproduces the observed spatial pattern reasonably well. The observations show that Baffin Bay also has high lead area fraction. The model does not capture leads in this area, however, due to the coarse resolution used. Note that the difference in the magnitude of different lead fraction observations is quite significant. This can be due to several reasons, including the different measurement techniques (active/passive, used frequencies and/or observational angles) and the different lead characteristics used for identification (thermal insulation/surface properties). Verifying these observations together in a systematic way needs a dedicated effort, which goes beyond the scope of this study.

Wintertime sea ice divergence obtained from RGPS is mainly available in the Canadian Basin (Fig. 2b). Within this area, Beaufort Sea stands out as a region of particularly strong sea ice divergence. While the model is able to consistently represent the observed spatial pattern of ice divergence, the magnitude is lower than the observed in the Beaufort Sea. Fig. 2 indicates that places with high simulated sea ice divergence are also regions with large simulated lead area fraction. This finding is consistent with the dynamical relationship between ice divergence and lead formation known from previous observations [*Miles and Roger*, 1998].

Time series of monthly mean sea ice divergence and lead area fraction averaged over Beaufort Sea are shown in Fig. 3a for the months when observations are available. Sea ice divergence shows pronounced variability, both on monthly and interannual time scales, which is very well reproduced by the model. The three observed lead fraction time series are largely consistent in terms of their variability, although there is difference in details for some of the years. The simulated lead fraction variability shows a relatively good agreement with the observed time series. Neither the observations nor the model simulation shows any evidence for significant trends in lead area fraction during the winter season. Further analysis indicates that this is true also for other Arctic regions (see Fig. S4 in the supplement).

In February 2013, a pronounced fracturing event occurred in the Beaufort Sea. This event, which has attracted considerable attention [*Beitsch et al.*, 2014; *Wernecke and Kaleschke*, 2015], was a result of strong storms leaving vast parts of the Beaufort Sea covered by leads. Hence, this event provides a good test case for assessing the fidelity of the high-resolution model. Fig. 3a shows that the model is capable of reproducing the anomalous sea ice conditions, given that the highest lead area fraction is simulated in March 2013 relative to the same months of the other years.

The fact that the model successfully simulates many of the observed features allows us to use the model results for an analysis of the sea ice lead variability. It turns out that on interannual time scales the simulated wintertime lead area fraction in Beaufort Sea is significantly correlated with the ice divergence (Fig. 3b). Furthermore, the correlation between ice divergence and wind velocity components at different direction has been calculated and the largest correlation coefficient is found for wind component in the direction about 74 degree to the northwest. At this direction the correlation coefficient amounts to 0.74. Finally, it is found that the correlation between ice divergence and sea level pressure (slp) is highest at the location of Beaufort High (see Fig. S5 in the supplement). Therefore, it can be concluded that a stronger (weaker) Beaufort High results in stronger (weaker) southeasterly offshore winds in Beaufort Sea and thus higher (lower) ice divergence and lead area fraction.

In contrast to the winter season, the model simulates significant trends in summer (Fig. 4): The sea ice shear and the lead area fraction show significant positive trends, whereas sea ice concentration shows the well-known decline. To better understand the relationship between summer lead area fraction and sea ice shear, their time series averaged in three regions are analyzed (Fig. 5a). The summer lead area fraction has increased by about 60–80% during the past three decades in these regions. Both its upward trends and interannual variability are closely linked to sea ice shear. In all these regions the trend and variability of ice shear is well anti-correlated with that of sea ice concentration (Fig. 5b).

Note that there are no summer lead fraction observation products for directly validating the model results.

Our analysis indicates that ice divergence does not significantly correlate with lead area fraction in summer (not shown). Although both ice divergence and shear contribute to ice deformation and can cause lead formation, the current model results indicate that ice divergence is the major cause of lead formation when ice concentration is close to 100% (in winter), while ice shear plays the major role in breaking sea ice when ice concentration and internal stress is low (in summer).

4. Discussion and conclusion

In this study, it is shown that sea ice models with traditional rheologies can reproduce certain characteristics of observed sea ice deformation and lead area fraction, including their spatial distribution and temporal variability, provided that horizontal resolution is sufficiently high (here 4.5 km) and numerical convergence is ensured. However, even a resolution of 4.5 km used here is not sufficient to model all aspects of real leads, many of which are typically much narrower [*Tschudi et al.*, 2002]. It is rather the resolution starting from which the models begin to demonstrate certain skill in representing the phenomenon.

The total sea ice deformation rate shows a power-law spatial scaling property in both our 4.5 km and 24 km resolution simulations (see Fig. S7 in the supplement), which is consistent with observations. In this regard our results are different from those by *Girard et al.* [2009]. The model results presented in our work are an important indication that there is hidden potential in traditional sea ice models with respect to modeling the small scale sea ice dynamics. The fact that our model is able to simulate Arctic leads with some skill opens new directions of scientific research. Examples include exploration of the climate relevance of leads; predictability of leads on daily to subseasonal time scales; and the impact of leads on the biogeochemistry of the Arctic ocean. At the same time, we acknowledge that there may be limitations to the assumptions underlying EVP/VP formulations and that new sea ice rheologies need to be explored [*Girard et al.*, 2011; *Tsamados et al.*, 2013; *Bouillon and Rampal*, 2015]. In fact, improving the fidelity of sea ice model dynamics is a timely and important topic.

Our simulation confirms that winter ice leads are mainly formed in marginal seas (Barents, Kara, Laptev and Beaufort Seas) and near Fram Strait. Confidence in the model results are enhanced by the fact that the model simulates the observed strong fracture event in Beaufort Sea in March 2013. The interannual variability of winter lead area fraction in Beaufort Sea can be largely explained by sea ice divergence variations, which are driven by southeasterly winds associated with variations in the strength of Beaufort High. The close relationship between wind speed, ice divergence and winter lead area fraction is also found in other Arctic regions (see Fig. S4 in the supplement), indicating that the wintertime lead area fraction variability can generally be explained by the variation of winds.

Summer ice velocity shear varies with the sea ice concentration and determines the interannual variability of lead area fraction. Decrease of sea ice concentration and internal stress facilitates stronger ice shear to break up sea ice, and this mechanism appears to be particularly important in summer. By exploring which component of the sea ice deformation rate can better explain the variability of lead area fraction over three decades of model results, ice divergence is found to be the main cause of lead formation when ice concentration is very high, while ice shear plays the major role in breaking sea ice when ice concentration is low. However, for an individual event or season, the relative contribution of ice divergence and shear to lead formation may departure from the above-mentioned relationship. More comprehensive studies on the linkage between lead formation and different sea ice deformation processes are still needed.

Our work shows that there is little evidence for the presence of significant trends in lead area fraction during wintertime. This is linked to the fact that Arctic wind stress has no significant trend so far. In summer, on the other hand, substantial positive trend in lead area fraction are found in the simulation. The trend is located where sea ice concentration is already low, so potential climate impacts of the trend are presumably less significant than winter trends would have been. It remains to be seen whether lead area fraction in winter will change in projected climate simulations.

In this paper we explored the importance of model resolution and EVP solver convergence. Many other aspects of the model, for example, advection schemes and parameterizations of sea ice thermodynamic processes, can also influence the model representation of sea ice leads. Furthermore, the resolution of the atmospheric forcing used in our work is coarse. Other atmospheric reanalysis data, especially those with higher resolution, need to be investigated in future work to understand the impact of different forcing on sea ice lead formation.

Acknowledgments. We thank the anonymous reviewers for their helpful comments. Q. Wang is funded by the Helmholtz Climate Initiative REKLIM (Regional Climate Change), a joint research project of the Helmholtz Association of German research centres (HGF). A. Wernecke is supported by ESA (Contract 4000112022/14/I-AM). L. Kaleschke is supported through the Cluster of Excellence CliSAP (EXC177), University of Hamburg, funded through the German Science Foundation (DFG). The simulation was performed at the North-German Supercomputing Alliance (HLRN). The model data used in plots are available upon request.

References

Beitsch, A., L. Kaleschke, and S. Kern (2014), Investigating high-resolution AMSR2 sea ice concentrations during the February 2013 Fracture Event in the Beaufort Sea, *Remote Sensing*, *6*, 3841–3856.

Bouillon, S., and P. Rampal (2015), Presentation of the dynamical core of neXtSIM, a new sea ice model, *Ocean Modelling*, *91*, 23–37.

Bouillon, S., T. Fichefet, V. Legat, and G. Madec (2013), The elastic-viscous-plastic method revisited, *Ocean Modelling*, *71*, 2–12.

Broehan, D., and L. Kaleschke (2014), A nine-year climatology of Arctic sea ice lead orientation and frequency from AMSR-E, *Remote Sensing*, *6*, 1451–1475.

Danilov, S., Q. Wang, R. Timmermann, N. Iakovlev, D. Sidorenko, M. Kimmritz, T. Jung, and J. Schroeter (2015), Finite-Element Sea Ice Model (FESIM), version 2, *Geoscientific Model Development*, *8*, 1747–1761.

Fily, M., and D. A. Rothrock (1990), Opening and closing of sea ice leads - digital measurements from synthetic aperture radar, *Journal of Geophysical Research-oceans*, *95*, 789–796.

Girard, L., J. Weiss, J. M. Molines, B. Barnier, and S. Bouillon (2009), Evaluation of high-resolution sea ice models on the basis of statistical and scaling properties of Arctic sea ice drift and deformation, *Journal of Geophysical Research-oceans*, *114*, C08,015.

Girard, L., S. Bouillon, J. Weiss, D. Amitrano, T. Fichefet, and V. Legat (2011), A new modeling framework for sea-ice mechanics based on elasto-brittle rheology, *Annals of Glaciology*, *52*, 123–132.

Herman, A., and O. Glowacki (2012), Variability of sea ice deformation rates in the Arctic and their relationship with basin-scale wind forcing, *The Cryosphere*, *6*, 1553–1559.

Hunke, E., and J. Dukowicz (1997), An Elastic-Viscous-Plastic model for sea ice dynamics, *J. Phys. Oceanogr.*, *27*, 1849–1867.

Hutchings, J. K., A. Roberts, C. A. Geiger, and J. Richter-Menge (2011), Spatial and temporal characterization of sea-ice deformation, *Annals of Glaciology*, *52*, 360–368.

Ivanova, N., P. Rampal, and S. Bouillon (2016), Error assessment of satellite-derived lead fraction in the Arctic, *The Cryosphere*, *10*, 585–595.

Jung, T., and co-authors (2016), Advanced polar prediction capabilities on daily to seasonal time scales, *Bulletin of the American Meteorological Society*, accepted, doi: 10.1175/BAMS-D-14-00246.1.

Kalnay, E., M. Kanamitsu, R. Kistler, W. Collins, D. Deaven, L. Gandin, M. Iredell, S. Saha, G. White, J. Woollen, Y. Zhu, A. Leetmaa, R. Reynolds, M. Chelliah,

W. Ebisuzaki, W. Higgins, J. Janowiak, K. C. Mo, C. Ropelewski, J. Wang, R. Jenne, and D. Joseph (1996), The NCEP/NCAR 40-Year Reanalysis Project, *Bull. Amer. Meteor. Soc.*, *77*, 437–471.

Kort, E. A., S. C. Wofsy, B. C. Daube, M. Diao, J. W. Elkins, R. S. Gao, E. J. Hintsa, D. F. Hurst, R. Jimenez, F. L. Moore, J. R. Spackman, and M. A. Zondlo (2012), Atmospheric observations of arctic ocean methane emissions up to 82 degrees north, *Nature Geoscience*, *5*, 318–321.

Kwok, R., A. Schweiger, D. A. Rothrock, S. Pang, and C. Kottmeier (1998), Sea ice motion from satellite passive microwave imagery assessed with ERS SAR and buoy motions, *Journal of Geophysical Research-oceans*, *103*, 8191–8214.

Kwok, R., E. C. Hunke, W. Maslowski, D. Menemenlis, and J. Zhang (2008), Variability of sea ice simulations assessed with RGPS kinematics, *Journal of Geophysical Research-oceans*, *113*, C11,012.

Lindsay, R. W. (2002), Ice deformation near SHEBA, *Journal of Geophysical Research-oceans*, *107*, 8042.

Lindsay, R. W., J. Zhang, and D. A. Rothrock (2003), Sea-ice deformation rates from satellite measurements and in a model, *Atmosphere-ocean*, *41*, 35–47.

Lindsay, R. W., K., and D. A. Rothrock (1995), Arctic sea-ice leads from Advanced Very High-resolution Radiometer Images, *Journal of Geophysical Research-oceans*, *100*, 4533–4544.

Lüpkes, C., T. Vihma, G. Birnbaum, and U. Wacker (2008), Influence of leads in sea ice on the temperature of the atmospheric boundary layer during polar night, *Geophysical*

Research Letters, *35*, L03,805.

Marcq, S., and J. Weiss (2012), Influence of sea ice lead-width distribution on turbulent heat transfer between the ocean and the atmosphere, *The Cryosphere*, *6*, 143–156.

Marsan, D., H. Stern, R. Lindsay, and J. Weiss (2004), Scale dependence and localization of the deformation of Arctic sea ice, *Physical Review Letters*, *93*, 178,501.

Maslowski, W., and W. H. Lipscomb (2003), High resolution simulations of Arctic sea ice, 1979-1993, *Polar Research*, *22*, 67–74.

Maykut, G. A. (1978), Energy exchange over young sea ice in central Arctic, *Journal of Geophysical Research-oceans and Atmospheres*, *83*, 3646–3658.

Miles, M. W., and R. G. Roger (1998), A 5-year satellite climatology of winter sea ice leads in the western Arctic, *Journal of Geophysical Research-oceans*, *103*, 21,723–21,734.

Moore, C. W., D. Obrist, A. Steffen, R. M. Staebler, T. A. Douglas, A. Richter, and S. V. Nghiem (2014), Convective forcing of mercury and ozone in the Arctic boundary layer induced by leads in sea ice, *Nature*, *506*, 81–84.

Onana, V.-D.-P., N. T. Kurtz, S. L. Farrell, L. S. Koenig, M. Studinger, and J. P. Harbeck (2013), A sea-ice lead detection algorithm for use with high-resolution airborne visible imagery, *Ieee Transactions On Geoscience and Remote Sensing*, *51*, 38–56.

Rampal, P., J. Weiss, and D. Marsan (2009), Positive trend in the mean speed and deformation rate of Arctic sea ice, 1979-2007, *Journal of Geophysical Research-oceans*, *114*, C05,013.

Roehrs, J., and L. Kaleschke (2012), An algorithm to detect sea ice leads by using AMSR-E passive microwave imagery, *The Cryosphere*, *6*(2), 343–352.

Sidorenko, D., T. Rackow, , T. Jung, , T. Semmler, D. Barbi, S. Danilov, K. Dethloff, W. Dorn, K. Fieg, H.F. Gling, D. Handorf, S. Harig, W. Hiller, S. Juricke, M. Losch, J. Schröter, D. Sein, and Q. Wang (2014), Towards multi-resolution global climate modeling with ECHAM6-FESOM. Part I: model formulation and mean climate, *Climate Dynamics*, *44*, 757–780.

Stern, H. L., and R. W. Lindsay (2009), Spatial scaling of Arctic sea ice deformation, *Journal of Geophysical Research-oceans*, *114*, C10,017.

Stone, R. S., and J. R. Key (1993), The detectability of Arctic leads using thermal imagery under varying atmospheric conditions, *Journal of Geophysical Research-oceans*, *98*, 12,469–12,482.

Tsamados, M., D. L. Feltham, and A. V. Wilchinsky (2013), Impact of a new anisotropic rheology on simulations of Arctic sea ice, *Journal of Geophysical Research*, *118*, 91–107.

Tschudi, M. A., J. A. Curry, and J. A. Maslanik (2002), Characterization of springtime leads in the Beaufort/Chukchi Seas from airborne and satellite observations during FIRE/SHEBA, *Journal of Geophysical Research-oceans*, *107*, 8034.

Wang, Q., S. Danilov, D. Sidorenko, R. Timmermann, C. Wekerle, X. Wang, T. Jung, and J. Schröter (2014), The Finite Element Sea Ice-Ocean Model (FESOM) v.1.4: formulation of an ocean general circulation model, *Geosci. Model Dev.*, *7*, 663–693.

Weiss, J., and D. Marsan (2004), Scale properties of sea ice deformation and fracturing, *Comptes Rendus Physique*, *5*, 735–751.

Wernecke, A., and L. Kaleschke (2015), Lead detection in Arctic sea ice from CryoSat-2: quality assessment, lead area fraction and width distribution, *The Cryosphere*, *9*, 1955–1968.

Willmes, S., and G. Heinemann (2015), Pan-Arctic lead detection from MODIS thermal infrared imagery, *Annals of Glaciology*, *56*, 29–37.

Willmes, S., and G. Heinemann (2016), Sea-Ice Wintertime Lead Frequencies and Regional Characteristics in the Arctic, 2003-2015, *Remote Sens.*, *8*, 4.

Figure 1. Simulated sea ice thickness on 1 January 2004 at model resolutions of (a) 4.5 km and (b) 24 km. The coarse model simulates a much smoother ice thickness field without the narrow lead-type structures obtained on the high resolution mesh. An animation of sea ice concentration and thickness on the 4.5 km mesh is available at `https://doi.pangaea.de/10.1594/PANGAEA.860354`. (c) Time series of lead area fraction in Beaufort Sea (the region indicated in the upper panels of Fig. 2) in four sensitivity runs on the 4.5 km resolution mesh, showing the importance of EVP solver convergence. In the figure legend, 'EVP' means the original *Hunke and Dukowicz* [1997] EVP method, and 'm-EVP' means the modified EVP version in which all the components of the stress tensor are relaxed to their viscous-plastic state at the same rate [*Danilov et al.*, 2015]. The values in the legend indicate the number of subcycling time steps used in the (m-)EVP solver. 'm-EVP 800' is the setting used in the analyzed simulation in our paper. The four experiments were started from the same initial condition obtained from 'm-EVP 800'.

Figure 2. (a) Mean sea ice lead area fraction [%] for the model (left), CryoSat-2 (middle) and MODIS (right) averaged from January to March of the period 2011–2014. (b) Mean sea ice divergence [0.001/day] for the model (left) and RGPS (right) averaged from January to April of the period 1997–2008. For the RGPS sea ice divergence, only those grid cells are shown that have data available for at least 2/3 of the record. The red boxes in (a) indicate the Beaufort Sea region used for the analysis shown in Fig. 3.

Figure 3. (a) Monthly-mean time series of sea ice divergence and lead area fraction in Beaufort Sea for the model (blue) and different observations (see legend). Only those months are shown for which observations are available. Simulated lead area fraction in March is highlighted by blue squares in the middel panel, and shown together with observations in the bottom panel, where each time series is normalized by subtracting its mean and devided by its standard deviation. (b) Simulated lead area fraction and sea ice divergence (upper panel) and sea ice divergence and the wind velocity component in the 'favourable' direction (i.e. -74° relative to the meridional direction) (lower panel) in Beaufort Sea. The time series in (b) are based on wintertime (January through March) means and normalized by their respective standard deviations. The averaging area used for Beaufort Sea is indicated in the upper panels of Fig. 2.

Figure 4. (a) Mean lead area fraction [%], ice shear [0.01/day] and sea ice concentration [%] for the summer months (July through September) of the period 1985 to 2014. (b) The linear trend of summer lead fraction [%/decade], ice shear [0.01/day/decade] and concentration [%/decade] for the period 1985–2014. For comparison the observed mean and trend of sea ice concentration is shown in Fig. S6 in the supplement.

Figure 5. (a) Normalized time series of lead area fraction and sea ice shear as well as (b) normalized time series of sea ice shear and concentration for summertime (July through September). The three average regions from left to right are indicated in Fig. 4b with indices 1 to 3, respectively. The calculation is done for those grid cells which have a sea ice concentration of at least 50%. The mean absolute values and the linear trends for each time series and their (detrended) correlation coefficients are shown in the corresponding panels. Values for lead fraction, ice shear and concentration have units [%], [0.01/day] and [%], respectively. The values of linear trends are shown for changes per decade. All the linear trends and correlations are significant at the 95% confidence level.

figure 1. Figure

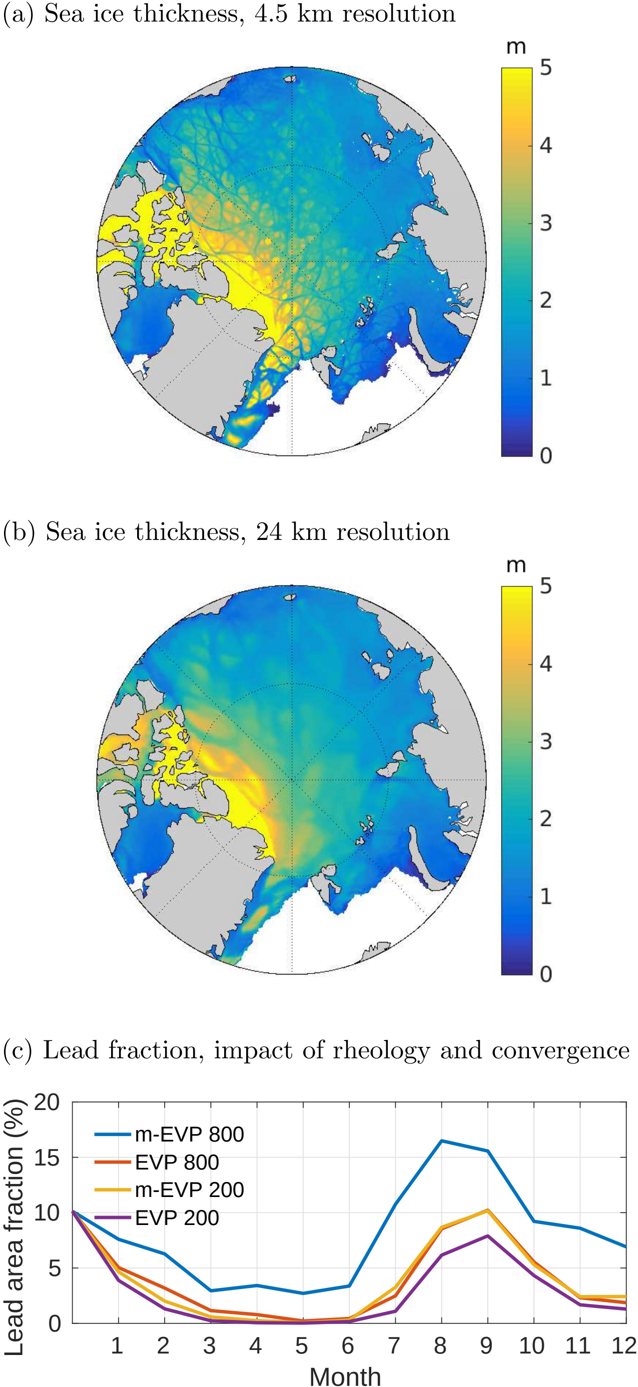
(a) Sea ice thickness, 4.5 km resolution
m
5
4
3
2
1
0
(b) Sea ice thickness, 24 km resolution
m
5
4
3
2
1
0
(c) Lead fraction, impact of rheology and convergence
Lead area fraction (%)
20
15
10
5
0
m-EVP 800
EVP 800
m-EVP 200
EVP 200
1
2
3
4
5
6
7
8
9
10
11
12
Month

figure 2. Figure

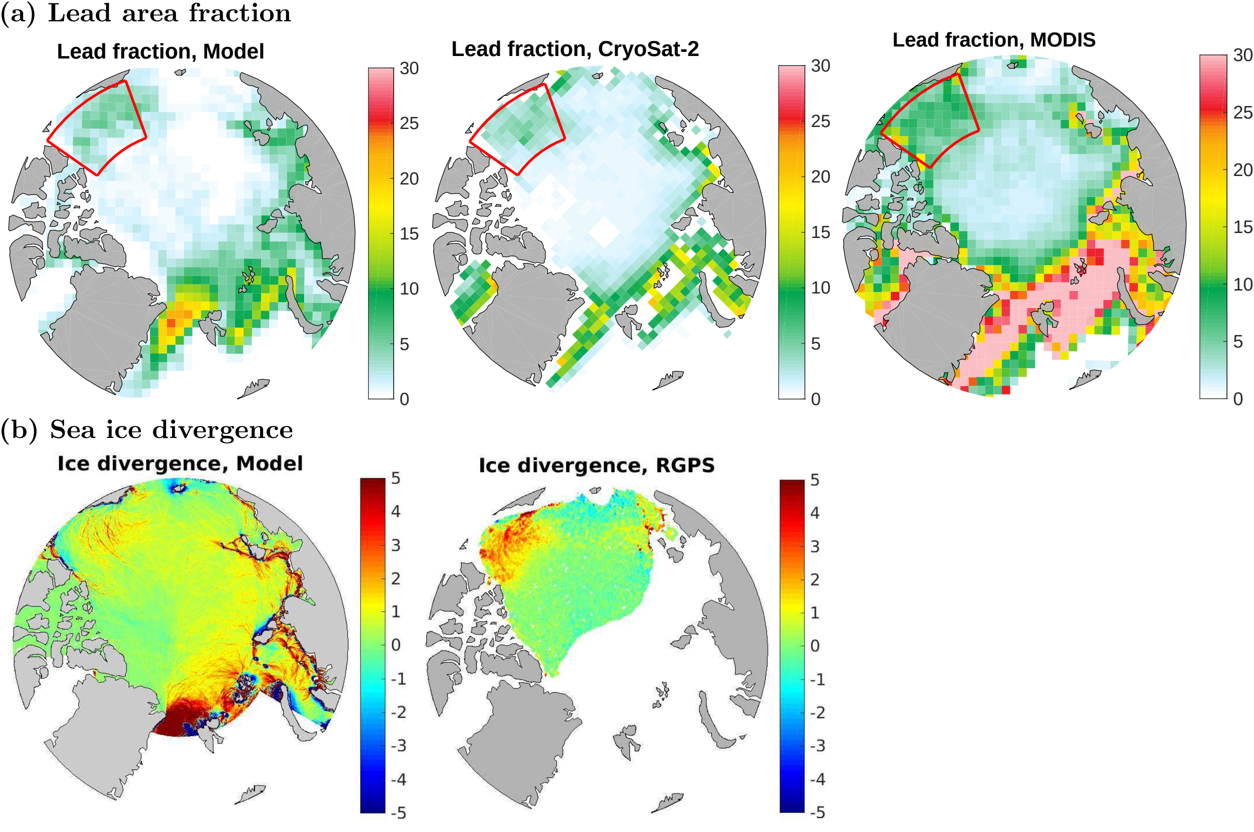
(a) Lead area fraction
Lead fraction, Model
Lead fraction, CryoSat-2
Lead fraction, MODIS
0
5
10
15
20
25
30
(b) Sea ice divergence
Ice divergence, Model
Ice divergence, RGPS
-5
-4
-3
-2
-1
0
1
2
3
4
5

figure 3. Figure

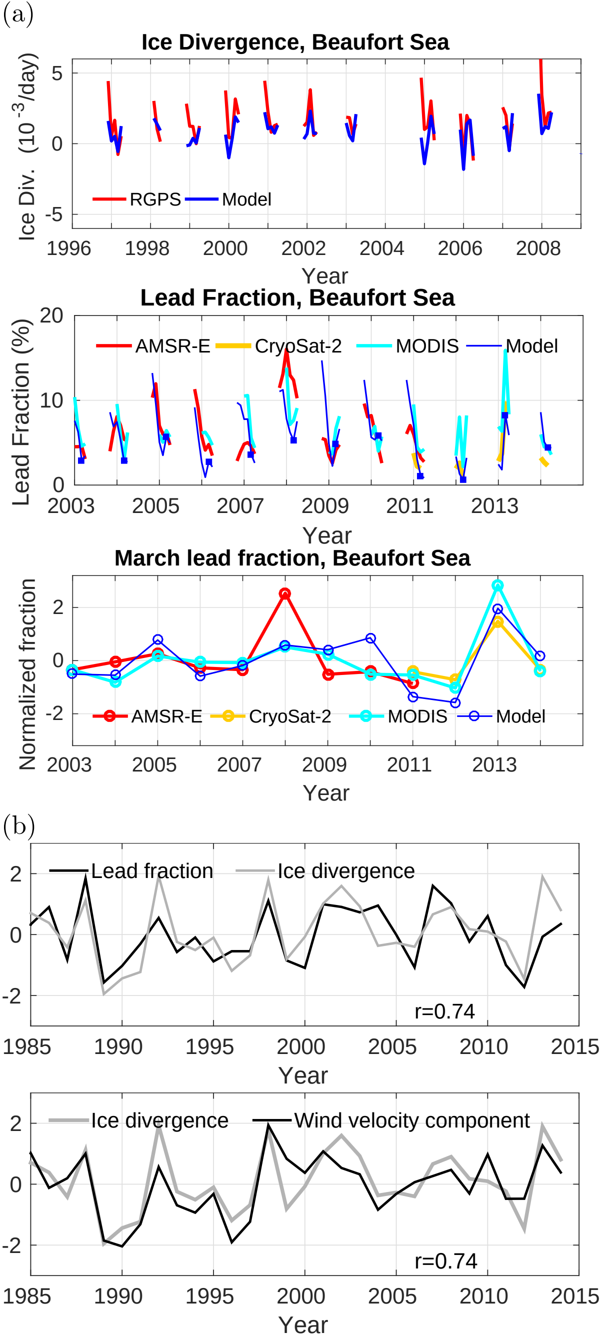
(a)
Ice Divergence, Beaufort Sea
Ice Div. (10^-3/day)
RGPS
Model
5
0
-5
1996
1998
2000
2002
2004
2006
2008
Year
Lead Fraction, Beaufort Sea
Lead Fraction (%)
AMSR-E
CryoSat-2
MODIS
Model
20
10
0
2003
2005
2007
2009
2011
2013
Year
March lead fraction, Beaufort Sea
Normalized fraction
AMSR-E
CryoSat-2
MODIS
Model
2
0
-2
2003
2005
2007
2009
2011
2013
Year
(b)
Lead fraction
Ice divergence
2
0
-2
r=0.74
1985
1990
1995
2000
2005
2010
2015
Year
Ice divergence
Wind velocity component
2
0
-2
r=0.74
1985
1990
1995
2000
2005
2010
2015
Year

figure 4. Figure

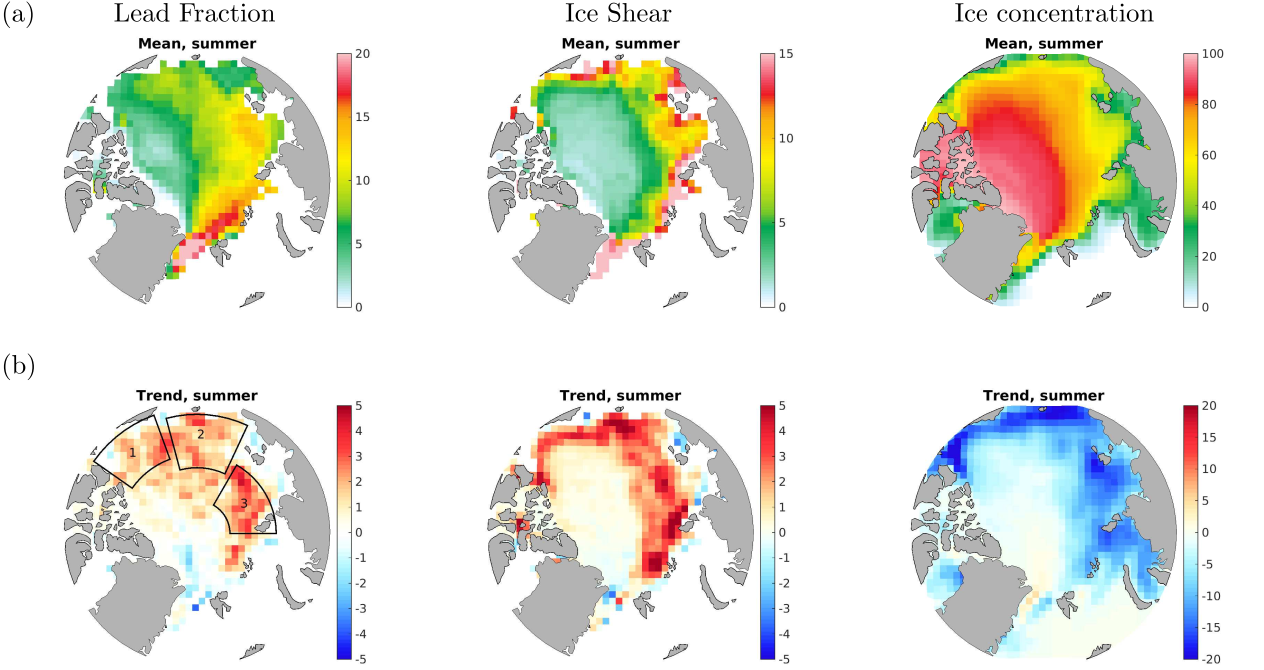

(a)
Lead Fraction
Ice Shear
Ice concentration
Mean, summer
Mean, summer
Mean, summer
(b)
Trend, summer
Trend, summer
Trend, summer
1
2
3

figure 5. Figure

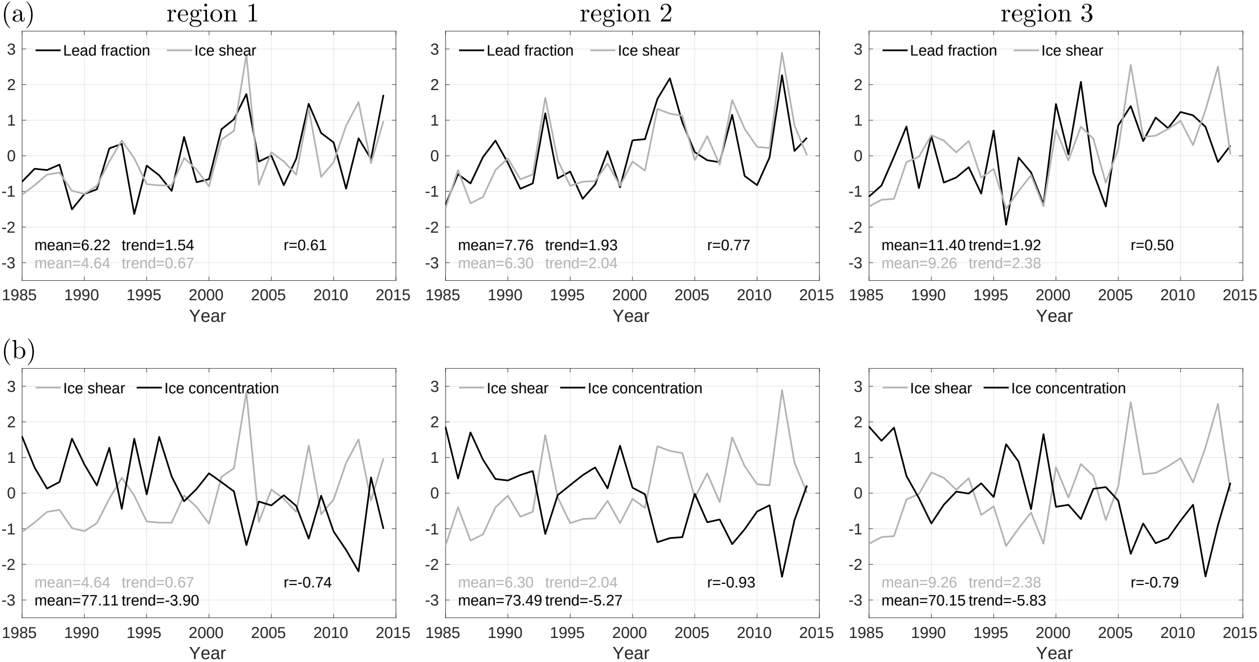
(a)
region 1
region 2
region 3
Lead fraction
Ice shear
mean=6.22 trend=1.54
mean=4.64 trend=0.67
r=0.61
mean=7.76 trend=1.93
mean=6.30 trend=2.04
r=0.77
mean=11.40 trend=1.92
mean=9.26 trend=2.38
r=0.50
Year
(b)
Ice shear
Ice concentration
mean=4.64 trend=0.67
mean=77.11 trend=-3.90
r=-0.74
mean=6.30 trend=2.04
mean=73.49 trend=-5.27
r=-0.93
mean=9.26 trend=2.38
mean=70.15 trend=-5.83
r=-0.79
Year